Granular Matter (2025) 27:32
https://doi.org/10.1007/s10035-025-01510-1

RESEARCH

A modular hypoplastic constitutive model for granular soils

Tim Pucker[1]

Received: 21 August 2024 / Accepted: 1 February 2025 / Published online: 14 February 2025

Abstract
A new hypoplastic constitutive model with a modular structure is presented for granular soils. The modular structure allows the application of the constitutive model with very little material information under restriction of the soil effects to be reproduced. The more material information available, the better the stress–strain behaviour of the material can be represented. The basic model and six modules are presented that allow to model soil phenomena like barotropy, pyknotropy, load history, and small strain stiffness. Laboratory tests are simulated to show the performance of the constitutive model.

Keywords Hypoplasticity · Soil model · Constitutive model · Material model · Small strain stiffness · Barotropy · Pyknotropy · Granular soil

1 Notation

The Voigt notation is used. The strain tensor $\boldsymbol{\varepsilon}$ is defined as:

$$\boldsymbol{\varepsilon} = (\varepsilon_{xx}, \varepsilon_{yy}, \varepsilon_{zz}, 2\varepsilon_{xy}, 2\varepsilon_{xz}, 2\varepsilon_{yz}) \tag{1}$$

The Cauchy stress tensor $\boldsymbol{\sigma}$ is defined as:

$$\boldsymbol{\sigma} = (\sigma_{xx}, \sigma_{yy}, \sigma_{zz}, \sigma_{xy}, \sigma_{xz}, \sigma_{yz}) \tag{2}$$

Calculations exclusively involve effective stresses; thus, a separate designation is omitted. The strain rate tensor is denoted by $\dot{\boldsymbol{\varepsilon}}$. Since the material time derivative of $\boldsymbol{\sigma}$ is not objective, the Jaumann stress rate is used, where $\boldsymbol{\omega}$ is the rotation rate of a co-moving observer measured by the temporal change of $\boldsymbol{\sigma}$. Hence Eq. (3) eliminates the influence of rigid body rotation on the stress rate. Fundamentally, a quasi-static state is assumed.

$$\mathring{\boldsymbol{\sigma}} = \dot{\boldsymbol{\sigma}} - \boldsymbol{\omega}\boldsymbol{\sigma} + \boldsymbol{\sigma}\boldsymbol{\omega} \tag{3}$$

✉ Tim Pucker
tim.pucker@hcu-hamburg.de

[1] Geotechnical Engineering, HafenCity University Hamburg, Henning-Voscherau-Platz 1, 20457 Hamburg, Hamburg, Germany

2 Introduction

Previous hypoplastic constitutive models [3, 12, 16, 17, 24] offer users little opportunity to intervene in the material equations used to specifically influence the depicted stress–strain behaviour. Mašin [14] developed a modular hypoplastic constitutive model that allows relatively easy modification of the elastic term L as well as the shape of the limit state surface. In this article, a new modular hypoplastic constitutive model is presented, which is intended to allow such interventions. The modular structure of the constitutive model aims to enable its application even with limited information of the geotechnical properties of a granular material. Only five material parameters are necessary to fundamentally work with the model. The more precisely the material behaviour is examined, the more parameters can be determined, and the modular extensions of the constitutive model can be used. This results in a more realistic representation of the material behaviour. The goal of the model formulation is to assign a clear phenomenon of granular soils to each material parameter. This way, the material parameters can be easily determined from the results of standard laboratory tests.

The modular structure is also intended to enable simple further development of the constitutive model. The modularly modelled phenomena can be considered, examined, and improved separately from the model, without the need to completely revise the constitutive model. Additionally, new modules can be added to the model to better represent the phenomena already included or to add new phenomena.

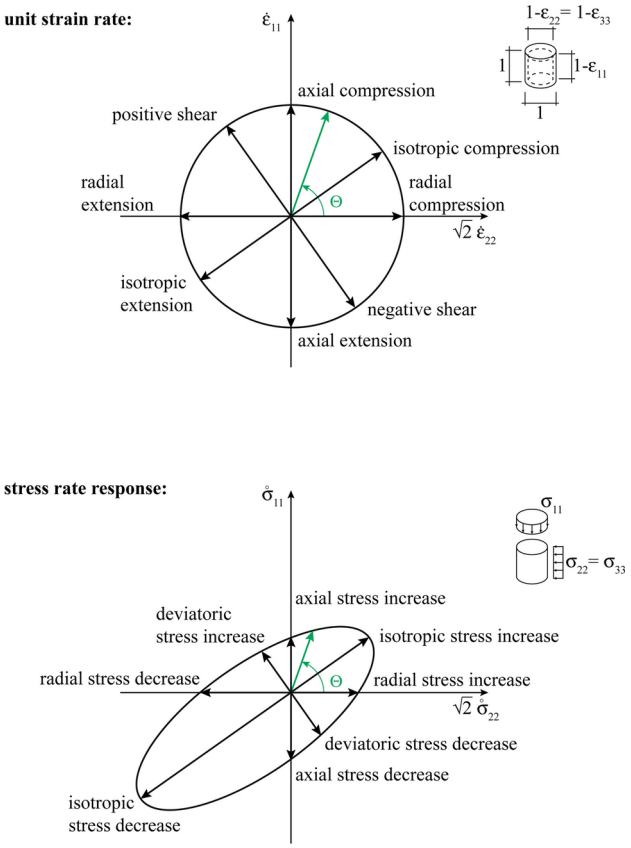

Fig. 1 Principle representation of the unit strain rate and the corresponding stress rate response; above: special directions of the unit strain rate; below: special directions of the stress rate response (modified after Gudehus [9])

The constitutive model can be classified within the group of hypoplastic constitutive models, as the material equation is of the rate type and corresponds to the generalized hypoplasticity according to Niemunis [17]. The structural development of the model is intended to be easily understandable for the user. Therefore, the material parameters and the parameters and designations used in the model are based on common geotechnical terms.

It is shown that the constitutive model can realistically reproduce the behaviour of granular soils under both drained and undrained conditions. For this purpose, laboratory tests are simulated to demonstrate the performance of the constitutive model.

2.1 Response envelopes

Gudehus [9] and Gudehus and Kolymbas [7] introduced the unit strain rate and the resulting unit response to evaluate the performance of constitutive models and to compare constitutive models with each other. According to Gudehus [9], the following assumptions are made:

Table 1 Direction designations of unit strain and stress rate response

Angle Θ	Direction designation	Direction designation
	Unit strain	Stress rate response
0.0°	Radial compression	Radial stress increase
35.3°	Isotropic compression	Isotropic stress increase
90.0°	Axial compression	Axial stress increase
124.3°	Positive shear	Deviatoric stress increase
180.0°	Radial extension	Radial stress decrease
215.3°	Isotropic extension	Isotropic stress decrease
270.0°	Axial extension	Axial stress decrease
305.3°	Negative shear	Deviatoric stress decrease

1. Only non-rotating deformations with cylindrical symmetry are examined. Due to the cylindrical symmetry, the stress state corresponds to triaxial conditions, and the stress σ_{22} is equal to the stress σ_{33}. Thus, the representation of the unit response in the Rendulic plane is possible. The stress directions are accordingly defined in Fig. 1.
2. The material behaviour is characterized by the stress rate response to a unit strain rate.

The unit strain rate is defined by Eq. (4).

$$\sqrt{\dot{\varepsilon}_{11}^2 + 2\dot{\varepsilon}_{22}^2} = 1 \tag{4}$$

The direction of the strain rate in the $\dot{\varepsilon}_{11} - \sqrt{2}\dot{\varepsilon}_{22}$ plane can be uniquely defined by the angle Θ, see Fig. 1 top.
The corresponding stress rate responses are determined for the different directions of the unit strain rates and are represented in the Rendulic plane, see Fig. 1 bottom. When many directions of the unit strain rate are evaluated, a circle forms in the $\dot{\varepsilon}_{11} - \sqrt{2}\dot{\varepsilon}_{22}$ plane. The stress rate responses form an ellipse-like shape in the Rendulic plane, which is why the stress rate response is often referred to as a stress ellipse or stress rate response ellipse. Special directions of the unit strain rate are listed in Table 1.

The representation in Fig. 1 allows the interpretation of the direction-dependent stiffness and the qualitative depiction of the material behaviour. An elliptical shape indicates that the stiffnesses of compression and shear differ. If the centre of the ellipse is shifted from the initial stress state, the stiffness in the direction of this shift is greater than in the opposite direction. From the stress rate response in Fig. 1, it can be concluded, that the unloading stiffness, with the exception of the deviatoric stress change, is always greater than the loading stiffness. By evaluating multiple stress rate response ellipses at different initial stress states, a constitutive model can also be examined for compliance with boundary conditions and its behaviour when approaching the boundary condition. This evaluation is presented in the

Rendulic plane of stresses and not of stress rates. Figure 2 shows the presentation principle. The advantage of this representation is that multiple initial stress states can be examined, and the behaviour of the constitutive model at different stress states can be assessed at a glance.

Scharinger and Schweiger [22] use stress rate response ellipses to assess the quality of constitutive models or to compare different models. If the strain rate is not specified but the stress rate is, strain rate response ellipses can be generated. Experimentally, strain and stress rates cannot be determined as they are infinitesimally small. Instead, strain response ellipses can be determined, which are generated by defined finite stress changes. Strain response ellipses are experimentally determined by Doanh [5] and compared with response ellipses calculated using the hypoplastic constitutive model by von Wolffersdorff [24]. Danne [4] experimentally determine strain response ellipses under low-cycle loading of non-cohesive soils. The numerical determination of strain response ellipses using the discrete element method (DEM) is shown by Froiio and Roux [6].

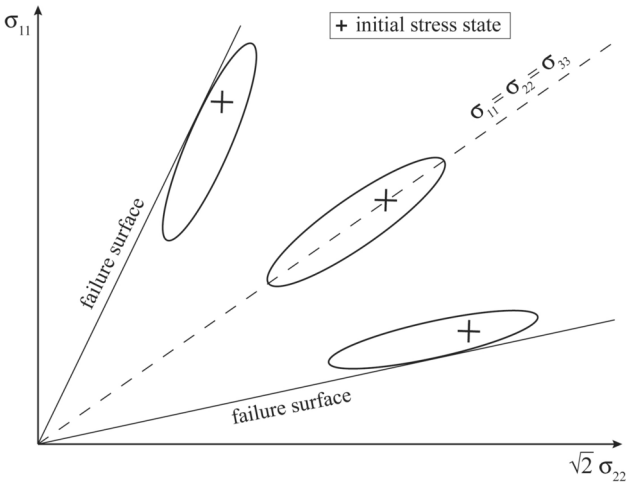

Fig. 2 Principal representation of multiple stress response ellipses in the Rendulic plane with failure surface and lines of mean pressure

3 Formulation of the constitutive model

3.1 Basic assumptions

1. It is assumed that a constitutive model can accurately describe the stress–strain-behaviour of soils if the stress response ellipses in the stress space can be realistically represented along with the corresponding stress paths.
2. The direction of the stress rate response is rotated by the angle ω with respect to the direction of the strain rate. The angle ω can be expressed by a function $\omega(\alpha)$, where α represents the angle between the direction of the strain rate $\dot{\boldsymbol{\varepsilon}}$ and the direction of the stress tensor $\boldsymbol{\sigma}$, see Fig. 3. The sum of the angles ω and α is referred to as β.
3. Furthermore, it is simplistically assumed that the stress rate response is velocity-independent.
4. Isotropic material behaviour is assumed.

3.2 Rotation of the stress rate response to the strain rate

The functional relationship between the rotation of the strain rate tensor to the stress tensor and the rotation of the stress rate response tensor to the strain rate tensor is derived based on some rotations from simple laboratory tests and theoretical considerations, see Pucker [20]. The strain rate in an oedometer test, for example, is uniaxial, so the angle α is predetermined (see Fig. 4). The corresponding stress

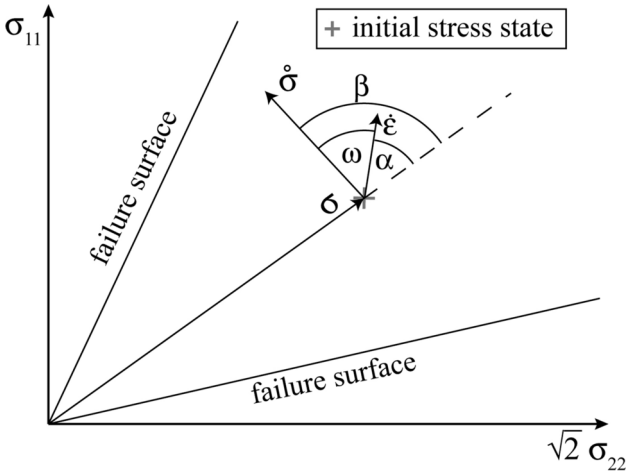

Fig. 3 Representation of the rotation of the stress rate response relative to the strain rate as a function of α

rate response, however, is multiaxial, and the angle β is therefore constrained between the angle of isotropic compression and triaxial compression. The angle β thus lies within a theoretical range from $0°$ (isotropic compression) to a maximum of $54.74°$ (triaxial compression). The angle $\beta = 54.74°$ for the direction of the stress rate response in drained triaxial compression results from the fact that the lateral pressures σ_{22} and σ_{33} do not change during drained triaxial compression. Therefore, the angle of the stress rate response is always $54.74°$, and only the magnitude of the stress rate response changes.

$$\cos\alpha = \frac{\dot{\boldsymbol{\varepsilon}} \cdot \boldsymbol{\sigma}}{\|\dot{\boldsymbol{\varepsilon}}\| \|\boldsymbol{\sigma}\|} \tag{5}$$

$$\cos\beta = \frac{\mathring{\boldsymbol{\sigma}} \cdot \boldsymbol{\sigma}}{\|\mathring{\boldsymbol{\sigma}}\| \|\boldsymbol{\sigma}\|} \tag{6}$$

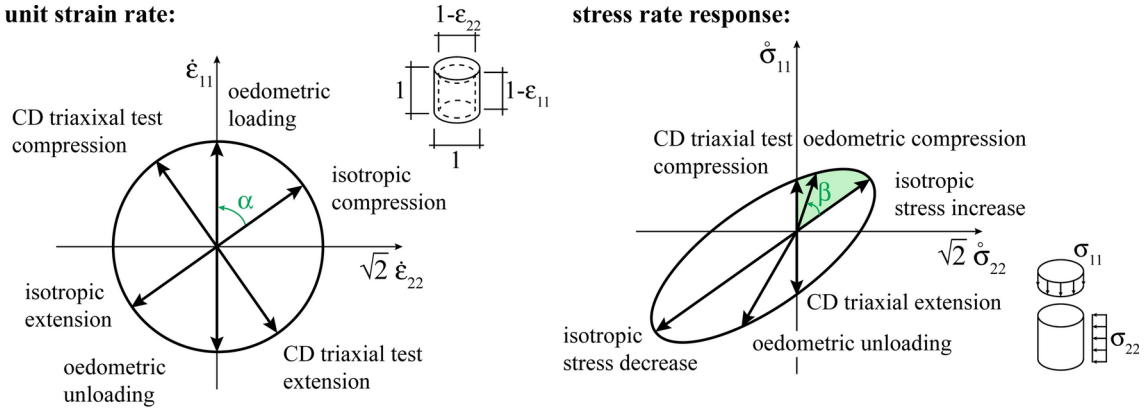

Fig. 4 Representation of the angles α in the Rendulic plane of the strain space and the angle β in the Rendulic plane of the stress space for an initial stress state on the axis of the mean pressure p

In Fig. 5, the results from conducted CD and CU triaxial tests, the theoretically possible ranges, and a possible approximation as a solid line in the diagram of the angle β over the angle α are presented. It is shown that the approximation intersects all theoretical ranges and some experimentally determined test results.

The mathematical approximation can be done, for example, using a sigmoid function, see Eq. (7). Equation (8) is the classic equation of a sigmoid function. By adding Equation (9)to Equation (7), Equation (8) is stretched such that β is always zero degrees at $\alpha = 0°$ and always $180°$ at $\alpha = 180°$. In this way, the theory of Goldscheider [8], which states that all stress paths tend towards a proportional stress path under isotropic stress states, is considered. In the present case, two sigmoid functions are used, each defined for $0 \leq \alpha \leq 180$ and $0 < \alpha - 180 < 180$. The proposed equation type allows for an accurate representation of the laboratory tests studied (see Fig. 5), but does not claim to be universally valid.

$$f(\alpha) = g(\alpha) + h(\alpha) \quad [\alpha \text{ in } °] \tag{7}$$

with:

$$g(\alpha) = \frac{a}{1 + e^{b(-\alpha+c)}} \tag{8}$$

$$h(\alpha) = \frac{180 - g(180) + g(0)}{180} \cdot \alpha - g(0) \tag{9}$$

The parameter a in Eq. (8) determines the maximum value of the sigmoid function and can generally be chosen as $a = 180$. The slope of the sigmoid function is controlled by the parameter b, and for the approximation shown, $b = 0.05$ was chosen. The parameter c determines the location of the inflection point of the sigmoid function, i.e., the angle between the strain rate tensor and the stress tensor at which the stress rate response tensor is perpendicular to the stress tensor. In the present example, $c = 90$ was chosen for $0 \leq \alpha \leq 180$ and $c = 110$ for $0 < \alpha - 180 < 180$ to best match the theoretical ranges and the experimental results. Since the functions with α or $\alpha_1 = \alpha - 180$ can always be defined for a range $0 \leq \alpha_1 \leq 180$, only the range $0 \leq \alpha \leq 180$ is considered in the following. The function $h(\alpha)$ ensures that the conditions $f(0) = 0$ and $f(180) = 180$ are met. By varying the parameters b and c, the function can be better adjusted if more experimental results are available. The influence on the stress strain behaviour for longer stress or strain paths is considered minor if all theoretical ranges are still intersected.

Furthermore, the condition must be met that an at-rest earth pressure coefficient K_0 is established during oedometer compression. To ensure this, the term Δ is added to Eq. 7. The term Δ can be determined by appropriate rearrangement of the material equation or approximated by Eq. 10 as a function of the effective friction angle φ'.

$$\Delta = 113.87\varphi'^{-0.1354} - 67.46 \quad [\varphi' \text{ in } °] \tag{10}$$

To determine the angle β, the result is given by Eq. 11.

$$\beta = f(\alpha) = g(\alpha) + h(\alpha) + \Delta \quad [\alpha \text{ in } °] \tag{11}$$

The angle ω, by which the strain rate tensor is rotated, can now be expressed by Eq. 12. The relationship is shown in Fig. 5 at the bottom.

$$\omega(\alpha) = f(\alpha) - \alpha \tag{12}$$

This approach is based on the theory of Goldscheider [8] applying his first and second rule on proportional stress paths. Nevertheless, experimental evidence for the mathematical expression is only shown for the hydrostatic stress state, see Fig. 5.

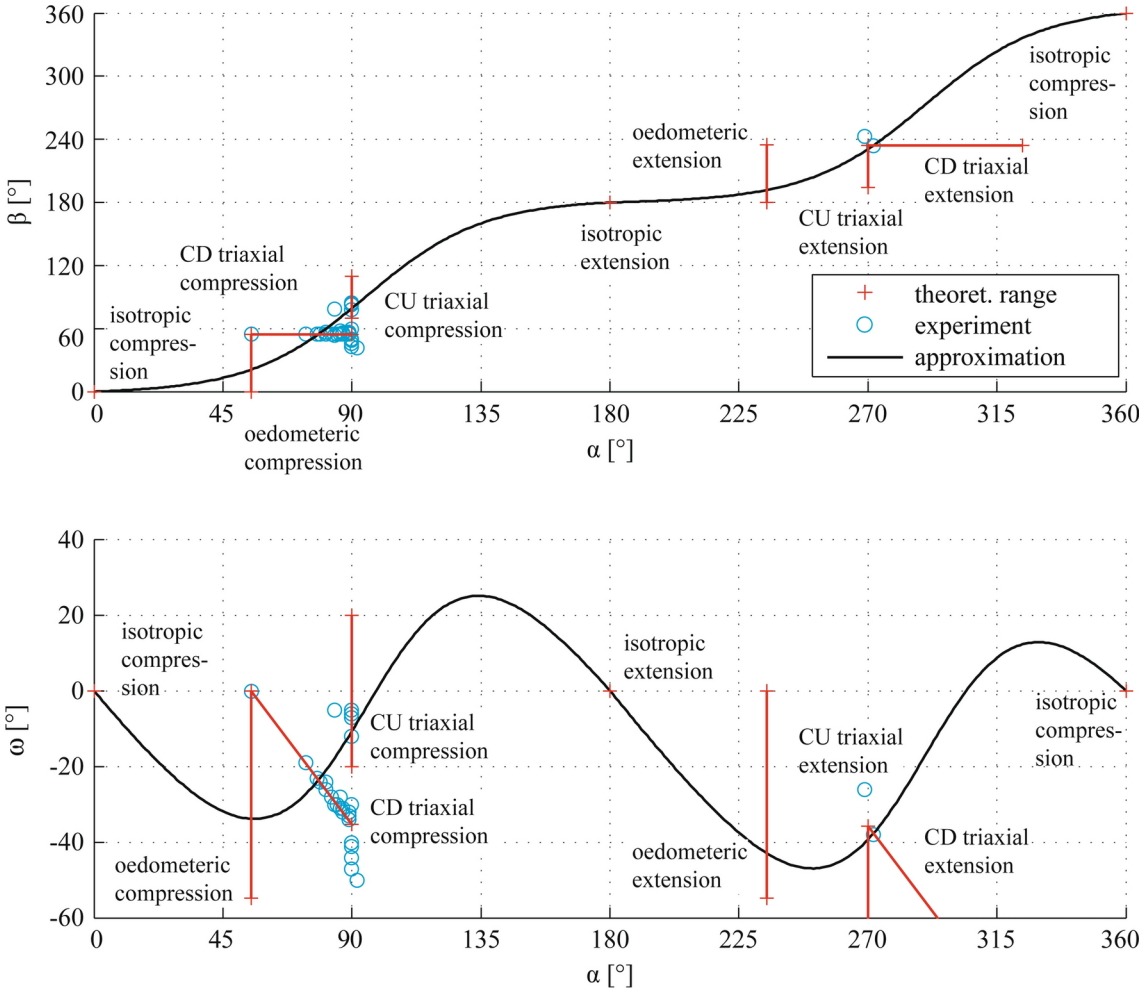

Fig. 5 Top: Representation of the relationship between the angle α between the stress tensor and the strain rate tensor and the angle β between the stress tensor and the stress rate response tensor with theoretically possible ranges, experimental data, and an approximation function at an initial stress point on the axis of the mean pressure p; Bottom: Representation of the relationship between the angle α between the stress tensor and the strain rate tensor and the angle ω between the strain rate tensor and the stress rate response tensor with theoretically possible ranges, experimental data, and an approximation function at an initial stress point on the axis of the mean pressure p

3.3 Basic structure

The basic structure of the constitutive model corresponds to the constitutive equation of generalized hypoplasticity according to Niemunis [17] and is expressed by Equation (13).

$$\overset{\circ}{\boldsymbol{\sigma}} = \boldsymbol{\mathcal{C}} : (\dot{\boldsymbol{\varepsilon}} - Y\boldsymbol{m}\|\dot{\boldsymbol{\varepsilon}}\|) \tag{13}$$

The mapping tensor $\boldsymbol{\mathcal{C}}$ of the 4th order mathematically represents the product of a rotation tensor $\boldsymbol{\mathcal{R}}$ and a stretching factor K^*. The flow direction $\boldsymbol{m}$ is added to the strain increment $\dot{\boldsymbol{\varepsilon}}$. The length of the flow direction is determined by the degree of nonlinearity Y and the norm of the strain increment $\dot{\boldsymbol{\varepsilon}}$. The term $(\dot{\boldsymbol{\varepsilon}} - Y\boldsymbol{m}\|\dot{\boldsymbol{\varepsilon}}\|)$ undergoes a rotation and a stretching by the mapping tensor $\boldsymbol{\mathcal{C}}$, resulting in a stress rate response tensor $\overset{\circ}{\boldsymbol{\sigma}}$.

The rotation angle is determined from Eq. (12), and the rotation axis is perpendicular to the direction of the strain increment and the direction of the stress tensor.

The stretching is determined by the stiffness of the material and depends on the mean pressure p and the void ratio e. Therefore, the void ratio e is introduced as a state variable, and the compression modulus K under isotropic loading is re-determined in each strain increment $\dot{\boldsymbol{\varepsilon}}$ using Eq. (14).

$$K = \frac{1+e}{C_{iK}} p \tag{14}$$

The isotropic compression coefficient C_{iK} is comparable to the compression coefficient C_C under oedometer loading. Assuming that a stress rate response ellipse in the Rendulic plane results from multiple unit strain increments, the compression modulus is varied depending on the angle β.

In the three-dimensional principal stress space, a stress rate response ellipsoid results from rotation around the direction of the stress tensor. The compression modulus K^* of the respective stress rate response tensor is thus determined depending on the direction of the stress rate response tensor (see Fig. 6) with an ellipse equation:

$$K_\perp = K \cdot \eta_K \tag{15}$$

$$K^* = \frac{K}{\sqrt{1 - \frac{K_\perp^2 - K^2}{K_\perp^2} \sin^2 \beta}} \tag{16}$$

The factor η_K corresponds to the ratio of the major axis lengths of the ellipse.

The rotation tensor $\boldsymbol{\mathcal{R}}$ is multiplied by the compression modulus K^*, resulting in the material tensor $\boldsymbol{\mathcal{C}}$:

$$\boldsymbol{\mathcal{C}} = K^* \cdot \boldsymbol{\mathcal{R}} \tag{17}$$

To ensure a change in stiffness when approaching the yield surface and compliance with this boundary condition, the term $Y \boldsymbol{m} \|\dot{\boldsymbol{\varepsilon}}\|$ is subtracted from the strain increment $\dot{\boldsymbol{\varepsilon}}$. The variable Y was introduced by Niemunis [17] to reformulate the hypoplastic basic equation, distinguishing between incremental linear elasticity at $Y = 0$ and unrestricted flow at $Y = 1$. Y is referred to as the degree of nonlinearity and describes the position of the stress relatively to the failure surface. Since the determination of the variable Y in this work does not follow exactly the formulation of Niemunis [17], the variable will be referred to as y in the further course of this work. In addition to the variable y, the flow direction $\boldsymbol{m}$ is introduced, in the direction of which the material flows unrestrictedly when the yield limit ($y = 1$) is reached. The tensor $\boldsymbol{m}$ is normalized as a unit tensor and multiplied by the norm of the strain increment tensor $\dot{\boldsymbol{\varepsilon}}$ to match the norm of the flow direction to the norm of the strain increment tensor. The flow direction in unrestricted flow ($y = 1$) is perpendicular to the yield surface in the critical state, and the trace of the flow direction is equal to one. The value of the variable y is determined using the yield condition according to Matsuoka and Nakai [15] based on the principal invariants of the stress tensor I_1, I_2, and I_3:

$$y = \left(\frac{-I_1 I_2}{I_3} - 9 \right) / \left(\frac{9 - \sin^2 \varphi'}{1 - \sin^2 \varphi'} - 9 \right) \tag{18}$$

The principal invariants are given by:

$$I_1 = \mathrm{trace}\,(\boldsymbol{\sigma}) \tag{19}$$

$$I_2 = \frac{1}{2} \left(\boldsymbol{\sigma} : \boldsymbol{\sigma} - I_1^2 \right) \tag{20}$$

$$I_3 = \det\,(\boldsymbol{\sigma}) \tag{21}$$

The flow direction is determined for the critical state, based on Niemunis [17]:

$$\boldsymbol{m} = \begin{cases} \dfrac{\hat{\boldsymbol{\sigma}}^*}{\|\hat{\boldsymbol{\sigma}}^*\|} & \text{for } \boldsymbol{\sigma} \leq -\mathbf{1} \\ \dfrac{1}{\sqrt{3}}\mathbf{1} & \text{for } \boldsymbol{\sigma} > -\mathbf{1} \end{cases} \tag{22}$$

with:

$$\hat{\boldsymbol{\sigma}}^* = \hat{\boldsymbol{\sigma}} - \frac{1}{3}\mathbf{1} \tag{23}$$

$$\hat{\boldsymbol{\sigma}} = \frac{\boldsymbol{\sigma}}{\mathrm{trace}(\boldsymbol{\sigma})} \tag{24}$$

The entries of the unit tensor $\mathbf{1}$ are $1_{ii} = 1$ and all other entries are zero.

3.3.1 Critical state

The volumetric behaviour of the soil is significantly determined by the void ratio e and its distance from the pressure-dependent critical void ratio e_c. Loose soils behave contractively under shear, while dense soils behave dilatively. This behaviour is represented in the constitutive model by introducing the mobilized dilatancy angle ψ'. The mobilized dilatancy angle ψ' causes a rotation of the flow direction, similar to non-associated flow rules in classical hyperplastic constitutive models. The dilatancy angle is determined by Eq. (25).

$$\tan \psi' = \tan \varphi' - \tan \varphi_c \tag{25}$$

The flow direction for the critical state (Eq. (22)) is rotated by the dilatancy angle ψ. The rotation axis is perpendicular

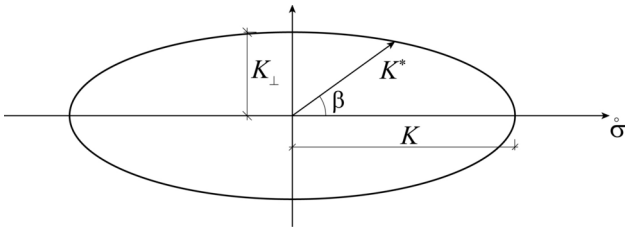

Fig. 6 Representation for determining the compression modulus K^*

to the flow direction $\boldsymbol{m}$ and the stress tensor $\boldsymbol{\sigma}$. For the flow direction, the resulting rotation tensor $\boldsymbol{\mathcal{R}}_\psi$ gives Eq. (26).

$$\boldsymbol{m} = \begin{cases} \boldsymbol{\mathcal{R}}_\psi \dfrac{\hat{\boldsymbol{\sigma}}^*}{\|\hat{\boldsymbol{\sigma}}^*\|} & \text{for } \boldsymbol{\sigma} \leq -\mathbf{1} \\ \dfrac{1}{\sqrt{3}}\mathbf{1} & \text{fo } \boldsymbol{\sigma} > -\mathbf{1} \end{cases} \tag{26}$$

3.3.2 Module 1: Pyknotropy and barotropy of the stiffness

The assumption of a constant compression coefficient C_C is only valid for some soft soils or is approximately valid within limited stress ranges, see for example Burland [2, Wood 25] and Kolymbas [13]. Granular soils typically exhibit a variable compression coefficient, which in turn depends on the stress state and the void ratio. Therefore, the isotropic compression coefficient C_{iK} is formulated as a function of the mean pressure p:

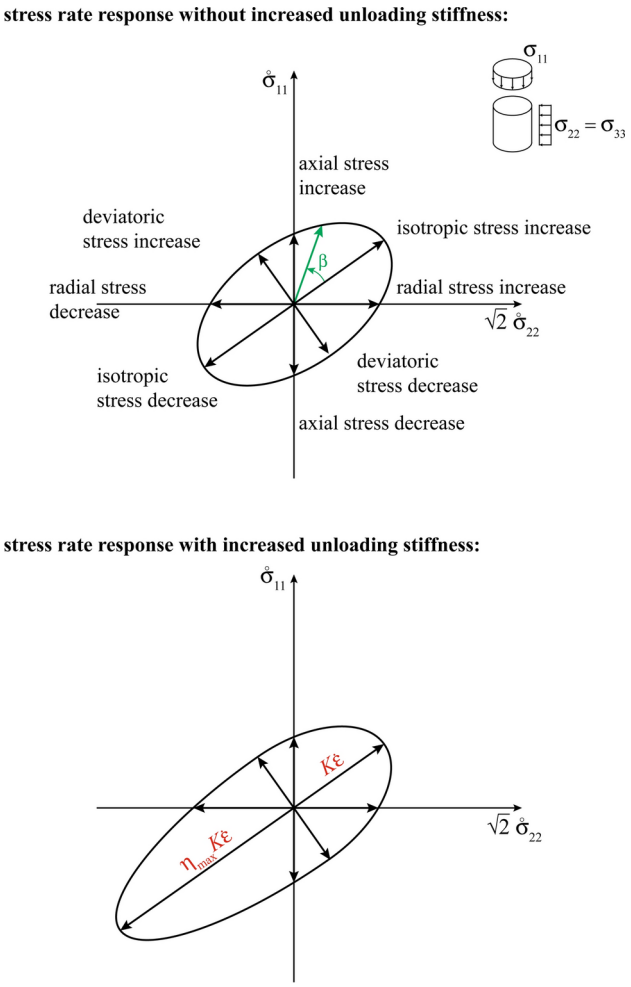

Fig. 7 Representation of the shape change of the stress ellipse to account for different loading and unloading stiffnesses

$$C_{iK} = C_{iK,0} \cdot \left(\frac{p}{p_0}\right)^{a_{C,iK}} \tag{27}$$

The reference pressure p_0 is a material parameter of the model and indicates the pressure at which some of the following material parameters were determined. This formulation corresponds to approach of Ohde [18], that the relationship between stiffness and stress can be expressed by a power law ($E_S \sim \sigma^a$). The parameters $C_{iK,0}$ is determined based on the void ratio to account for the pyknotropic nature of the stiffness:

$$C_{iK,0} = C_{iK,00} \cdot \left(\frac{e}{e_c}\right)^{b_{C,iK}} \tag{28}$$

From Eqs. (27) and (28), the additional required material parameters for this module are derived: $e_{c,0}$ (critical void ratio at reference stress p_0), $C_{iK,00}$ (isotropic compression coefficient at reference pressure p_0), $a_{C,iK}$ and $b_{C,iK}$. Equations (27) and (28) were developed based on several laboratory investigations on various sands, see Pucker [19].

3.4 Module 2: Directional dependence of stiffness

To describe the directional dependence of stiffness, the term "directional dependence" must first be defined more precisely. In soil mechanics, this term generally refers to the distinction between loading, unloading, and reloading. Generally, the loading direction already differs between axial and isotropic compression, although both represent a loading condition. In the basic formulation, the constitutive model is formulated as strain-direction dependent and the stiffness already depends on the loading direction. This module specifically addresses the effect of different stiffnesses observed in laboratory tests during loading, unloading, and reloading.

A higher unloading stiffness is already implemented into the constitutive model due to its hypoplastic formulation. The ellipse is enlarged in the unloading direction by a factor $\eta_{\max}$, see Fig. 7:

$$\eta_{\max} = \frac{C_{unloading}}{C_{loading}} = \frac{1-y}{1+y} \tag{29}$$

While the hypoplastic formulation does not implicitly account of an increased reloading stiffness, Equation (16) is redefined in sections, see Equation (30), and the factor $\eta_{\max}$ is implemented for the reloading case. However, the function of the stress ellipse remains continuously differentiable, as the stiffness $K_\perp$ does not change during deviatoric stress increase and decrease.

$$K^* = \begin{cases} \dfrac{K}{\sqrt{1 - \dfrac{K_\perp^2 - K^2}{K_\perp^2} \sin^2 \beta}} \\ \dfrac{\eta_{\max} K}{\sqrt{1 - \dfrac{K_\perp^2 - (\eta_{\max} K)^2}{K_\perp^2} \sin^2 \beta}} \end{cases} \quad \text{if} \quad \cos\beta > 0 \,\text{and}\, e \geq e_v \tag{30}$$

Equation (30) implies the introduction of the preloading void ratio e_v to indicate up to which void ratio e the soil was preloaded. The preloading void ratio e_v corresponds to the void ratio e during loading and remains constant during unloading. During reloading, the preloading void ratio remains constant until the void ratio e matches the preloading void ratio e_v and then decreases accordingly with the void ratio e. Thus, the preloading void ratio e_v can only decrease or remain constant during a calculation. This behaviour is observed only during axial or isotropic loading, unloading, and reloading. On the other hand soils can "forget" their preloading history through shearing. Therefore, the preloading void ratio e_v in the model can also increase through shearing and in turn "forget" parts of the preloading history. If the stress state reaches the yield surface and the soil behaves dilatively, the preloading void ratio e_v increases according to the void ratio change Δe caused by dilatancy. Similar principles are used e.g. in the Modified Cam Clay model, see Wood [25]. The preloading void ratio e_v in step $i+1$ is thus:

$$e_v^{i+1} = \begin{cases} e & \text{if} \quad e^{i+1} < e_v^i \quad \text{(loading)} \\ e_v^i & \text{if} \quad e^{i+1} \geq e_v^i \quad \text{and} \quad y < 1 \quad \text{(unloading/reloading)} \\ e_v^i + \Delta e & \text{if} \quad e^{i+1} \geq e_v^i \quad \text{and} \quad y \geq 1 \quad \text{(dilatant shearing)} \end{cases} \tag{31}$$

3.5 Module 3: Deviatoric stiffness

The stiffness of soils under triaxial loading or shearing depends on the distance of the stress state from the yield surface. The closer the stress state is to the yield surface, the softer the soil behaves in this loading direction. The formulation of the constitutive model according to Eq. (13) already represents this behaviour. However, this behaviour cannot yet be controlled by a material parameter depending on the respective soil material.

It is assumed that the size of the ellipse decreases as it approaches the boundary condition. This behaviour is also represented by other hypoplastic models, see Chambonet al. [3, Tamagnini et al. 23] and Niemunis [17]. This effect is implemented to the presented constitutive model by reducing the ratio of the major axis length of the ellipse η_K (see Eq. (15)) as it approaches the boundary condition:

$$\eta_K = \eta_{iK} - y\,(\eta_{iK} - 0.2) \tag{32}$$

The ratio η_{iK} corresponds to the ratio of the major axis lengths for isotropic initial stress states. The minimum ratio η_K is limited to $\eta_K = 0.2$ according to Eq. (32) to ensure a unique stress rate response is determined. At $\eta_K = 0$, the stress rate response ellipse would become a line, and the stress rate response is no longer uniquely associated with a strain rate. Thus, the shape of the stress response ellipse can be adjusted according to the real material behaviour. Herle and Kolymbas [10] use this method to adapt a hypoplastic model for representing soils with small friction angles.

3.6 Module 4: Pyknotropy of shear strength

The effective friction angle in granular soils mainly depends on the density and the stress state. Only a constant effective friction angle φ' is considered according to Eq. (18). In this module, the constitutive model is therefore extended by a state-dependent friction angle. It is assumed that the pressure dependence of the friction angle can be approximately expressed by the ratio of the critical void ratio e_c to the void ratio e, as the critical void ratio itself is pressure-dependent, see e.g. Wood [25]. The friction angle is therefore expressed as a function of e_c/e, see Eqs. (33) and (34).

$$\varphi(e_r) = 0,035 e_r^{a_\varphi} + \varphi_c - 0,035 \qquad \text{with } \varphi_c \text{ in rad} \tag{33}$$

with:

$$e_r = \frac{e_c}{e} \tag{34}$$

The pressure dependence of the critical void ratios is determined according to the approach from Module 1:

$$e_c = e_{c,0} - C_{iK} \ln\left(\frac{p}{p_0}\right) \tag{35}$$

The angle φ_c is a material parameter and corresponds to the critical friction angle at the critical void ratio $e_{c,0}$. The exponent a_φ is a material parameter that determines the course of the friction angle depending on the relative void ratio e_r . The limit value of the friction angle function is assumed to be 0, 035, respectively 2°, below the critical friction angle to model contractive behaviour during increasing shear of a sample of overcritically loose soil with a void ratio $e > e_c$. The formulation in Eq. (33) for considering the pyknotropy of shear strength can be used in Eq. (25) to calculate the mobilized dilatancy angle ψ. This makes it possible to distinguish between contractive and dilative material behaviour depending on the void ratio. Since the critical friction angle is a material parameter with Module 4, the effective friction angle is determined for each void ratio using Eq. (33).

3.7 Module 5: Cohesion

Since the constitutive model is not intended to be used exclusively for representing granular and therefore largely cohesionless soils, another module is introduced to account for cohesive behaviour. The yield surface according to Matsuoka and Nakai [15] is shifted along the axis of the mean pressure by the value Δp to represent the cohesive behaviour of soils. Cohesion c' is introduced as a material parameter, and the value of Δp is determined according to Eq. (36).

$$\Delta p = 2c' \frac{(3 - \sin\varphi')}{(6 \sin\varphi')} \tag{36}$$

3.8 Module 6: Small strain stiffness

Small strain stiffness is introduced to the model using approach presented in Santosand Correira [21] that is also implemented in the hardening soil small strain model [1]. The approach describes the relationship between the maximum shear modulus G_0 at small strains, the shear modulus G, the shear strain γ and the shear strain $\gamma_{0.7}$ at $G/G_0 = 0.70$ (Eq. (37)).

$$\frac{G}{G_0} = \frac{1}{1 + 0.385 \left(\frac{\gamma}{\gamma_{0.7}} \right)} \tag{37}$$

It is assumed that the small strain stiffness is proportional to the compression modulus K and the same formulation can be used to considered the barotropy and the pyknotropy of the small strain stiffness. Hence, the compression modulus K in Eq. (14) is multiplied with a factor F_{K0K} to obtain the small strain compression modulus (Eq. (38)). Replacing G with K and G_0 with K_0 in Eq. (37) and limiting the minimum stiffness to K, the stiffness of the constitutive model is increased at small strain ranges.

$$f_{K0K} = \frac{G_0}{G} = \frac{K_0}{K} \tag{38}$$

$$K = \max \left(\left[\frac{1}{1 + 0.385 \left(\frac{\gamma}{\gamma_{0.7}} \right)} f_{K0K};\ \ 1 \right] \right) \cdot \frac{1 + e_0}{C_{iK}} p \tag{39}$$

Two material parameters, f_{K0K} and $\gamma_{0.7}$ as well as two additional state parameters $\dot{\boldsymbol{\varepsilon}}_{t-1}$ and γ_{hist} are needed for consideration of the small strain stiffness.

The state parameter $\dot{\boldsymbol{\varepsilon}}_{t-1}$ matches the previous strain increment and is used to calculate a change in loading direction. The state parameter γ_{hist} represents the accumulated strain magnitude in the loading direction of $\dot{\boldsymbol{\varepsilon}}_{t-1}$. If the loading direction changes compared to the previous strain increment, the state parameter γ_{hist} is changed to account for an increased stiffness due to the change of the loading direction. At reversed loading, the state parameter γ_{hist} is set to zero resulting in a full recovering of the small strain stiffness. As stated in Niemunis [17] the small strain stiffness is only partially recovered if the loading direction is changing less than reverse. This effect is taken into account by setting γ_{hist} to a value that corresponds to the desired increase in stiffness. The relationship between change in direction and stiffness recovery is described by the co-sinus function given in Eq. (40). γ_{hist} is updated according to Eq. (41).

$$f_{G0} = \max \left(\left[\frac{1}{F_{K0K}};\ \ 0.5 + \frac{\dot{\boldsymbol{\varepsilon}} \dot{\boldsymbol{\varepsilon}}_{\boldsymbol{t-1}}}{\|\dot{\boldsymbol{\varepsilon}}\| \|\dot{\boldsymbol{\varepsilon}}_{t-1}\|} \cdot 0.5 \right] \right) \tag{40}$$

$$\gamma_{hist} = \min \left(\left[\gamma_{hist};\ \ \frac{1 - f_{G0}}{0.385 f_{G0}} \gamma_{0.7} \right] \right) \tag{41}$$

4 Material parameters

The material model can be used in its basic formulation with five material parameters. In the complete formulation with all presented modules, the determination of a total of eleven material parameters is necessary, which can mainly be obtained from standard laboratory tests. Table 2 provides an overview of the material parameters and alternative values of the module parameters for deactivating the respective modules.

5 Inspection of the constitutive model

The presented modular hypoplastic constitutive model is examined for its properties to identify potential weaknesses of the model. Figures 8 and 9 show the results of simulated element tests considering all the presented modules. This representation is referred to as the fingerprint of a constitutive model, as it provides a quick impression of the capabilities of a constitutive model.

Figure 8 (top) shows the results of an oedometer test with a loosely packed sample and an oedometer test with a densely packed sample. Figure 8 (top left) displays the determined stress–strain curves, and Fig. 8 (top right) shows the corresponding stress paths. It is shown that the constitutive model reproduces different stiffnesses depending on the packing density and the direction of loading.

Fig. 8 (middle) presents the results of four CD triaxial tests at initial stress states of 50 and 100 kPa with both

Table 2 Material parameters with their description and alternative values for deactivating individual modules

No	Symbol	Module	Description	Alt. Value
1	p_0	–	Reference pressure [kPa]	–
2	$e_{c,0}$	–	Critical void ratio at p_0 [-]	–
3	η_{iK}	–	Stress ratio between deviatoric stress change and isotropic compression at $q = 0$ [-]	–
4	$C_{iK,00}$	–	Isotropic compression coefficient at p_0 [-]	–
5	φ_c	–	Critical friction angle at $e_{c,0}$ / Effective friction angle if module 4 is not used [°]	–
6	$a_{C,iK}$	1	Exponent for barotropic stiffness [-]	0
7	$b_{C,iK}$	1	Exponent for pyknotropic stiffness [-]	0
8	a_φ	4	Exponent for pyknotropic shear strength [-]	0
9	c	5	Cohesion [kPa]	0
10	f_{K0K}	6	Fraction of maximum small strain stiffness G_0 to stiffness G	1
11	$\gamma_{0.7}$	6	shear strain $\gamma_{0.7}$ at $G/G_0 = 0.70$	0

loosely and medium-densely packed samples. The stress–strain curves are shown in Fig. 8 (middle left), and the volumetric strain-strain curves are shown in Fig. 8 (middle right). The model distinguishes between contraction and dilation depending on the packing density. Furthermore, the dependence of shear strength on the relative density and stress state is demonstrated.

The results of simulated CU triaxial tests in Fig. 8 (bottom) at initial stress states of 50 and 100 kPa with both loosely and medium-densely packed samples show realistic stress–strain paths (Fig. 8 bottom left) and characteristic stress paths in the deviatoric plane for densely packed soils (Fig. 8 bottom right). The mean stress decreases with increasing shear in loosely packed samples and increases in densely packed samples. However, in real soils with loosely packed samples, the decrease in mean stress begins at smaller deviatoric stresses, as seen in Ishihara [11]. Therefore, the undrained shear strength in very loosely packed soils is overestimated. This can lead to unsafe results in stability analyses and must be considered when evaluating the outcomes.

In Fig. 9 (top), the results of drained simple shear tests at constant confining pressure are presented. The stress–strain curves are shown in Fig. 9 (top left), and the volumetric strain-strain curves are shown in Fig. 9 (top right). The results exhibit the same properties as the CD triaxial test results. The model distinguishes between dilation and contraction, and shear strength depends on the stress state and packing density.

A drained cyclic simple shear test considering ten cycles is presented in Fig. 9 (middle). While the stress strain paths are shown in Fig. 9 (middle left) the change of the void ratios are presented in Fig. 9 (middle right). The initially dense samples is loosened due to cyclic shearing while the initially loose sample is densified. The degree of loosening or densification depends on the amplitude of the shear strain. This theoretical mechanical behaviour is typical for hypoplastic constitutive models while it has not been observed in lab tests (see e.g.Youd [26]). The change in shear strength with changing void ratio can is shown in Fig. 9 (middle left). For the initially dense sample, the maximum shear stress σ_{12} per cycle has the highest value at the first loading path and decreases with each cycle.

The stress ellipses in Fig. 9 (bottom left) demonstrate that the yield surface is not exceeded. The elliptical shape of the stress rate responses and their reduction as they approach the yield surface are evident.

The stress vectors in Fig. 9 (bottom right) show characteristic stress responses of the soil. None of the depicted stress paths exceeds the yield surface.

Stress paths from simulated cyclic undrained triaxial tests are shown in Fig. 10. The tests are simulated for an initially loose sample (Fig. 10 left) and an initially dense sample (Fig. 10 right). The initial isotropic stress is $p' = 200$ kPa and the cyclic loading amplitude is $\Delta q = \pm 25$ kPa. The cyclic loading of the loose sample causes a reduction of the mean stress p'. After a few cycles the effective stresses become zero, hence the soil liquefies. The mean stress p' is also reduced due to the cyclic loading of the dense sample, but the mean stress remains larger than zero. Soil liquefaction does not occur. Instead a so called butterfly pattern is simulated by the constitutive model.

6 Comparison to real soil behaviour

To demonstrate the performance of the material model on a real soil, the material parameters for the so-called Wundersand [19] were calibrated. The material parameters are listed in Table 3.

6.1 Oedometric compression test

Two oedometer tests are conducted at different densities. The very loosely packed sample has an initial void ratio of $e_0 = 0.77$ and the densely packed sample has an initial void ratio of $e_0 = 0.53$. The vertical stress before the actual test begins is $\sigma_{11} = 15{,}5$ kPa caused by the loading platen contacting the sample. Both samples are loaded up

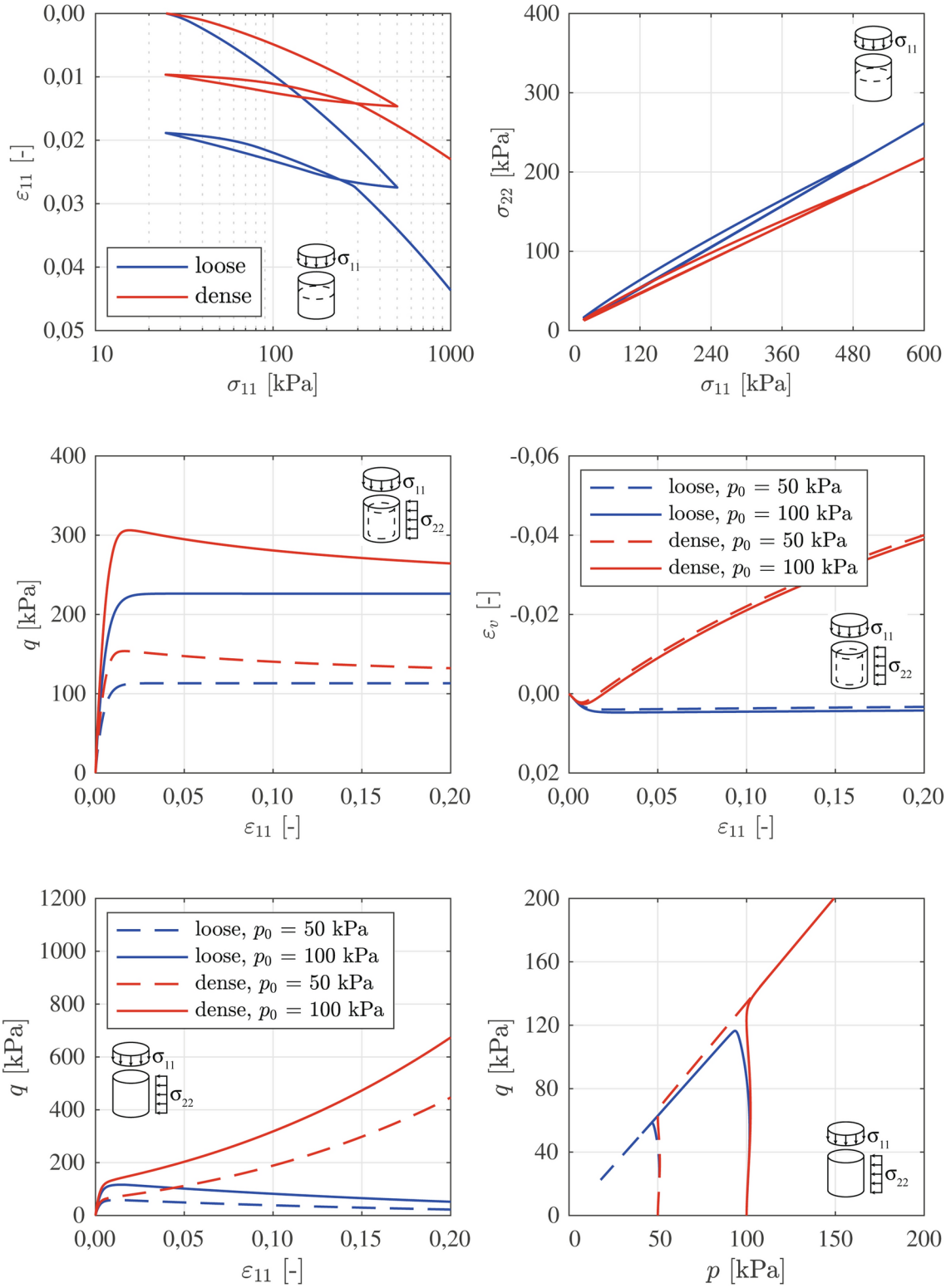

Fig. 8 Fingerprint of the constitutive model; top: oedometer tests on densely and loosely packed samples with loading, unloading, and reloading; middle: loosely and densely packed samples in drained triaxial tests at 50 kPa and 100 kPa cell pressure; bottom: loosely and densely packed samples in undrained triaxial tests at 50 kPa and 100 kPa cell pressure

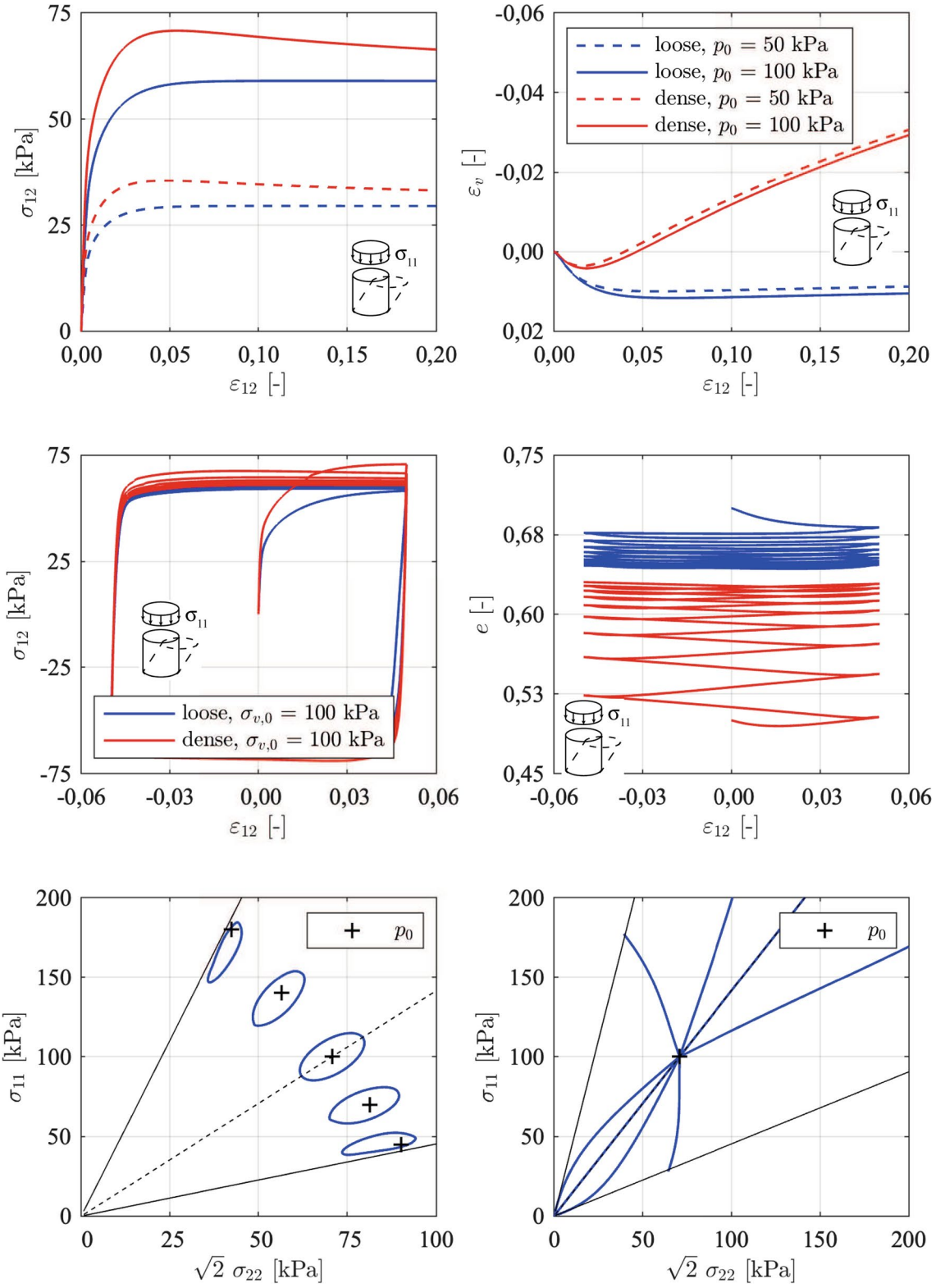

Fig. 9 Fingerprint of the constitutive model; top: loose and dense samples in drained simple shear tests at 50 and 100 kPa cell pressure; middle: loose and dense samples in cyclic drained simple shear tests at 100 kPa cell pressure; bottom left: stress ellipses in the Rendulic plane; bottom right: stress paths in the Rendulic plane

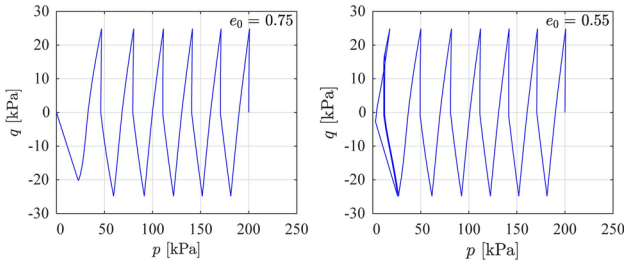

Fig. 10 Fingerprint of the constitutive model; top: loose and dense samples in drained simple shear tests at 50 and 100 kPa cell pressure; middle: loose and dense samples in cyclic drained simple shear tests at 100 kPa cell pressure; bottom left: stress ellipses in the Rendulic plane; bottom right: stress paths in the Rendulic plane

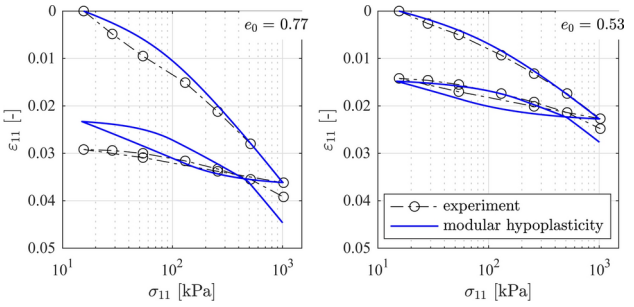

Fig. 11 Stress–strain diagram of two oedometer tests with numerical analysis; left: loosely packed sample; right: densely packed sample

to $\sigma_{11} = 1000$ kPa and then unloaded to $\sigma_{11} = 15{,}5$ kPa unloaded. Subsequently, a reloading up tos $\sigma_{11} = 1000$ kPa. follows. The results of the oedometer tests and a numerical analysis are shown in Fig. 11.

It is evident that the stress–strain paths during loading are well represented at both densities. The different stiffnesses in each direction are accurately reproduced. The unloading stiffness is slightly overestimated for the densely packed sample. The stress–strain paths during reloading are well represented, taking into account the unloading phase.

6.2 Drained triaxial compression test

A total of nine drained triaxial tests were simulated using the material model. The samples were installed in the test apparatus at loose, medium-dense, and dense packing and consolidated at an effective cell pressure of 100, 200, and 400 kPa, respectively. Subsequently, the cell pressure was kept constant, and the sample was sheared to failure through vertical strain. The initial void ratio e_0 s 0.63 for loose packing, 0.54 for medium-dense packing, and 0.46 for dense packing. The results of the experiments and the simulated CD triaxial tests are shown in Fig. 12 for loosely packed samples, Fig. 13 for medium-dense samples, and Fig. 14 for densely packed samples.

The shear strength, stiffness of the soil, and volume change of the samples are well represented in the simulation of drained triaxial tests for samples ranging from loosely to densely packed (see Figs. 12, 13 and 14). The volume change of the sample in the contraction range is underestimated for loosely packed samples. For medium-dense and densely packed samples, the volume change is better represented than for loosely packed samples; however, the dilatancy at higher strains is underestimated in densely packed samples. The peak shear strength is realistically represented for tests with densely packed samples, although the softening of the material is underestimated (see Fig. 14 left). The behaviour of granular soils in CD triaxial tests, including the effects of contraction, dilatancy, and barotropic and pyknotropic shear strength, can be represented by the material model.

Table 3 Material parameters for Wundersand

Material- parameter	p_0 [kPa]	$e_{c,0}$ [-]	η_{iK} [-]	$C_{iK,00}$ [-]	φ_c [°]	$a_{C,ik}$ [-]	$b_{C,iK}$ [-]	a_φ [-]	c [kPa]	f_{K0K} [-]	$\gamma_{0.7}$ [-]
Value	100	0.70	0.50	0.005	32	0.08	1.35	3.85	0	6	$3e^{-4}$

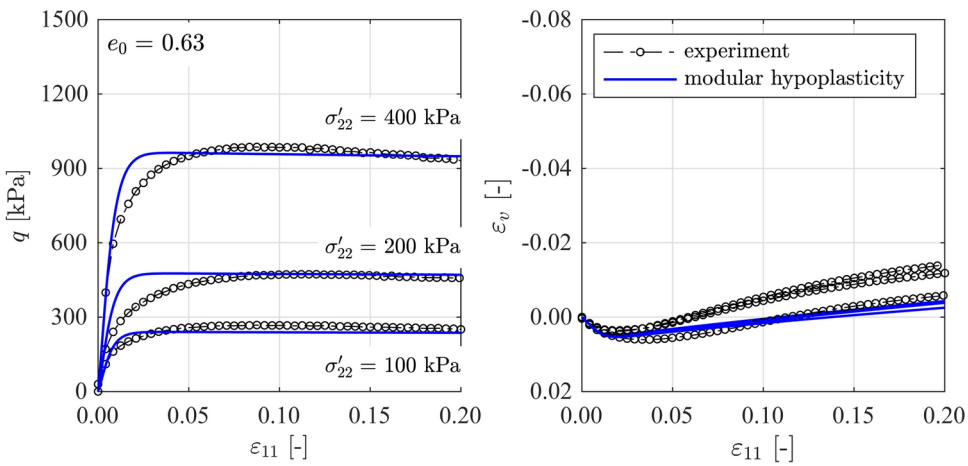

Fig. 12 Simulation of drained triaxial tests on loosely packed samples at three different cell pressures

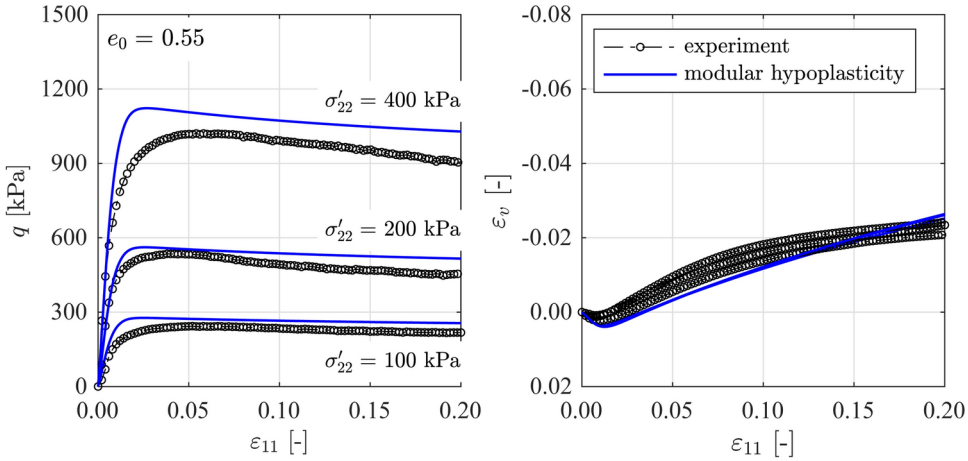

Fig. 13 Simulation of drained triaxial tests on medium-dense samples at three different cell pressures

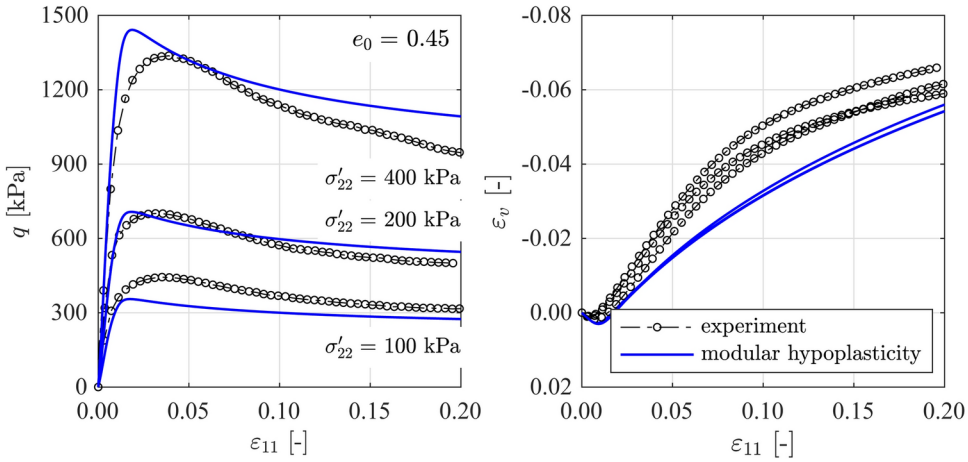

Fig. 14 Simulation of drained triaxial tests on dense samples at three different cell pressures

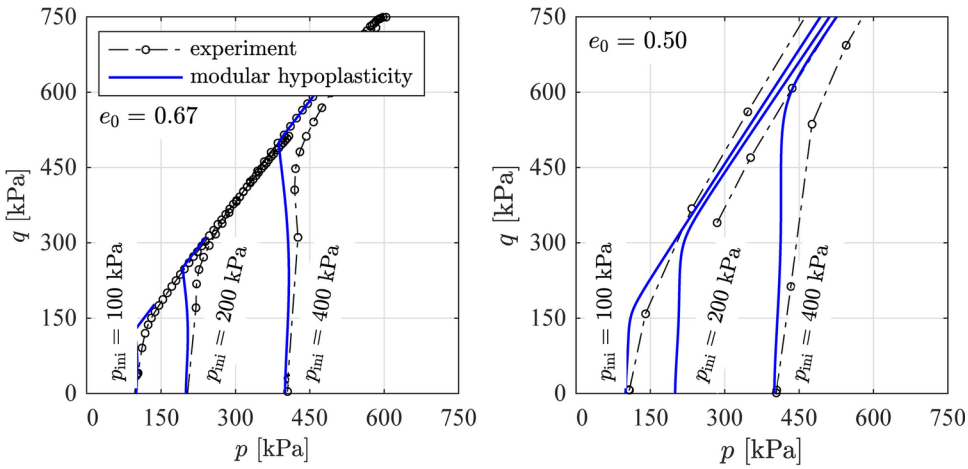

Fig. 15 Simulation of undrained triaxial tests on loose and dense samples at intermediate initial stress states of 100, 200, and 400 kPa

6.3 Undrained triaxial compression

The behaviour of the material model under undrained triaxial conditions is demonstrated with the results from six undrained triaxial tests (CU). In Fig. 15, the left side shows the stress paths from three CU triaxial tests with loose packing under three different initial stress states. The packing is slightly denser than the critical state, which explains the increase in mean pressure upon reaching the boundary condition. It is shown that the stress paths are realistically represented, and a critical state is reached where the mean stress and deviatoric stress remain constant. The results from the densely packed tests shown on the right side of Fig. 15 indicate that the stress paths are also realistically represented in terms of stiffness and behaviour upon reaching the boundary condition for densely packed samples. It is assumed that a

critical state will also be reached in densely packed samples; however, this is not shown in Fig. 15, as the critical state is expected to occur only at a very high mean pressure.

7 Conclusion

The modular hypoplastic constitutive model presented in this paper offers the possibility to use the model already with only limited information about the soil properties. Once the information about the soil properties increases, additional modules of the constitutive model can be activated, resulting in a much more realistic representation of the mechanical behaviour of granular soils. The model can reproduce the effects of barotropy and pyknotropy of the material stiffness and shear strength. Additionally the loading history is reflected by introducing increased stiffnesses in unloading and reloading cases. Besides this effect, the constitutive model is able to forget parts of the loading history due to dilative shearing. The phenomena of small strain stiffness is implemented to the model as well.

The model allows for simulation of the mechanical behaviour of granular soils under monotonic and also under cyclic loading. The capabilities of the model are shown by simulating standard laboratory tests.

Funding Open Access funding enabled and organized by Projekt DEAL.
This research received no specific grant from any funding agency in the public, commercial, or not-for-profit sectors.

Declarations

Conflict of interest The author has no Conflict of interest.

References

1. Benz, T.: Small-strain stiffness of soils and its numerical consequences,. PhD thesis, Mitteilungen des Instituts für Geotechnik der Universität Stuttgart , Mitteilung 55 (2007)
2. Burland, J.B.: On the compressibility and shear strength of natural clays. Géotechnique **40**, 329–378 (1990)
3. Chambon, R., Desrues, J., Charlier, R., Hammad, W.: Cloe, a new rate type constitutive model for geomaterials: theoretical basis and implementation. Int. J. Numer. Anal. Meth. Geomech. **18**(4), 253–278 (1994)
4. Danne, S., Hettler, A.: Verhalten von nichtbindigen Böden bei niederzyklischer Belastung. Geotechnik **36**, 19–28 (2013)
5. Doanh, T.: Strain response envelope: a complementary tool for evaluating hypoplastic constitutive equations. In: Kolymbas, D. (ed.) Constitutive Modelling of Granular Materials, pp. 375–396. Springer, Berlin, Heidelberg (2000)
6. Froiio, F., Roux, J.-N.: Incremental response of a model granular material by stress probing with DEM simulations. In: IUTAM-SIMM Symposium on Mathematical Modelling and Physical Instances of Granular Flow (2009). https://doi.org/10.1063/1.3435388
7. Gudehus, G., Kolymbas, D.: A constitutive law of the rate type for soils. In: Wittke, W. (ed.) Proc. Third International Conference on Numerical Methods in Geomechanics, vol. 1. Aachen, pp. 319–329 (1979)
8. Goldscheider, M.: Grenzbedingung und Fliessregel von Sand. Mech. Res. Commun. **3**, 463–468 (1976)
9. Gudehus, G.: A comparison of some constitutive laws for soils under radially symmetric loading and unloading. In: Wittke, W. (ed.) Proc. Third International Conference on Numerical Methods in Geomechanics, vol. 4, pp. 1309–1323. Aachen (1979)
10. Herle, I., Kolymbas, D.: Hypoplasticity for soils with low friction angles. Comput. Geotech. **31**, 365–373 (2004)
11. Ishihara, K.: Liquefaction and flow failure during earthquakes. Géotechnique **43**(3), 351–451 (1993). https://doi.org/10.1680/geot.1993.43.3.351
12. Kolymbas, D.: A rate-dependent constitutive equation for soils. Mech. Res. Commun. **4**, 367–372 (1997)
13. Kolymbas, D.: Geotechnik, 3rd edn. Springer, Berlin (2011)
14. Mašin, D.: Clay hypoplasticity with explicitly defined asymptotic states. Acta Geotech. **8**, 481–496 (2013)
15. Matsuoka, H., Nakai, T.: A new failure for soils in three-dimensional stresses. In: Proceedings IUTAM - Symposium on Deformation and Failure of Granular Materials, pp. 253–263 (1982)
16. Niemunis, A., Herle, I.: Hypoplastic model for cohesionless soils with elastic strain range. Mech. Frict. Cohes. Mater. **2**, 279–299 (1997)
17. Niemunis, A.: Extended hypoplastic models for soils. Habilitation, Veröffentlichungsreihe des Instituts für Grundbau und Bodenmechanik der Ruhr-Universität Bochum, Heft 34 (2003)
18. Ohde, J.: Zur Theorie der Druckverteilung im Baugrund. Der Bauingenieur, 451–459 (1939)
19. Pucker, T.: Stoffmodell zur Modellierung von stetigen Materialübergängen im Rahmen der Optimierung geotechnischer Strukturen,. PhD thesis, Veröffentlichungen des Instituts für Geotechnik und Baubetrieb der TU Hamburg-Harburg, Heft 28 (2013)
20. Pucker, T.: A response envelope based approach to hypo plastic constitutive models. In: Proc. of the 8th European Conference on Numerical Methods in Geotechnical Engineering, Delft, pp. 91–96 (2014)
21. Santos, J.A., Correira, A.G.: Reference threshold shear strain of soil. its application to obtain a unique train-dependent shear modulus curve for soil. In: Proc. 15th Int. Conf. SMGE, vol. 1. A.A. Balkema, pp. 267–270 (2001)
22. Scharinger, F., Schweiger, H.: Response envelopes of a multilaminate model for soils. Numerical Models in Geomechanics - NUMOG IX, 151–156 (2004)
23. Tamagnini, C., Viggiani, G., Chambon, R.: A review of two different approaches to hypoplasticity. In: Kolymbas, D. (ed.) Constitutive Modelling of Granular Materials, pp. 109–145. Springer, Berlin (2000)

24. von Wolffersdorff, P.-A.: A hypoplastic relation for granular materials with a predefined limit state surface. Mech. Frict. Cohes. Mater. **1**, 251–271 (1996)
25. Wood, D.M.: Soil Behavior and Critical State Mechanics. Cambridge University Press, Cambridge (1990)
26. Youd, T.L.: Compaction of sands by repeated shear straining. J. Soil Mech. Found. Div. **98**, 709–725 (1972)